JMES The International Journal of
Mechanical Engineering and Sciences
https://iptek.its.ac.id/index.php/jmes
e-ISSN 2580-7471

Comparative Dimensional Accuracy of Dovetail and Airfoil EDM Defect on Gas Turbine Blades Using Camera Image and Micrometer

Maulana Yusuf Izzuddin[1], Sampurno[1*], Muhammad Thaliban Habib Hudzaifah Na'im[1], Muhammad Rafi Kalevi[2], Bismaka Adhipramana Pinggala[3]

[1]Department of Mechanical Engineering, ITS, Sukolilo Surabaya 60111, Indonesia
[2]Process Safety Engineering, ITS, Sukolilo Surabaya 60111, Indonesia
[2]PT. Sumi Rubber Indonesia

Received: 26 February 2026, Revised: 05 March 2026, Accepted: 05 March 2026

Abstract

Gas turbine blades experience severe thermo-mechanical loading; therefore, dimensional examination of damage features must be accurate, repeatable, and non-destructive. This study develops and validates a non-contact digital image processing workflow to quantify artificial defects produced by die-sinking electrical discharge machining (EDM) on two blade regions with distinct surface characteristics: a serrated dovetail joint and a smooth airfoil. Six defects were manufactured (three per region) with nominal depths of 0.5, 1.0, and 2.0 mm. Repeatability was assessed using 20 measurements per defect (120 total) to determine accuracy via relative error and precision via standard deviation, followed by non-parametric and variance testing, and validation against a 0.001 mm resolution digital micrometer. Planar dimensions (length and width) achieved 97.5-99.9% accuracy, with overall accuracy above 95% and no significant difference in median accuracy between regions ($P = 0.577$). Precision was significantly lower on the dovetail ($P < 0.001$), attributed to serration-driven shadows and specular reflections that degrade edge stability. Micrometer comparisons showed minimal deviation for straight-line features, while airfoil measurements captured a more representative two-dimensional projected profile than chord-based contact readings. The results demonstrate a rapid, low-cost, and surface-safe inspection approach, while highlighting optical constraints that must be controlled to ensure consistent metrology on complex turbine geometries.

Keywords: Gas Turbine Blade, EDM, Image Processing, Non-contact Inspection

1. Introduction

Gas turbine blades are essential components in gas-fired power plant systems, responsible for converting the thermal energy generated by combustion into mechanical energy. This mechanical energy rotates the turbine shaft, facilitating electricity production. These turbine blades operate under extremely high thermomechanical stress; thus, maintaining their geometric integrity is crucial to prevent failures and ensure operational efficiency [1–5]. In high-reliability components, service life is closely linked to the evolution of mechanical properties during service, which further motivates early defect detection and quantification [6]. To address these challenges, accurate and precise inspection strategies are required to detect geometric imperfections, as well as the slightest damage or defects. To facilitate rigorous maintenance strategies, the industry increasingly relies on non-contact inspection systems [7, 8]. In parallel, data-driven modeling and optimization methods (e.g., hybrid BPNN-GA frameworks) are increasingly applied in machining to improve multi-performance characteristics and support sustainable manufacturing decisions [9]. Consequently, calibration blocks containing artificial defects are required to verify the accuracy and reliability of these inspection tools [10, 11]. These artificial defects are typically manufactured using Die-Sinking Electrical Discharge Machining (EDM) due to its capability to machine complex geometries and hard materials with high precision [12]. However, manufacturing these defects on turbine blades presents a unique challenge due to the blade's complex variation in surface curvature. The blade geometry is characterized by intricate features, ranging from dovetail to the contoured airfoil area [13]. The calibration block will subsequently be sectioned using wirecut Electrical Discharge Machining (EDM) to produce specimens suitable for microstructural analysis via scanning electron microscopy (SEM).

While accurate manufacturing is vital, validating the geometry of these artificial defects is equally critical. Non-contact methods, such as digital image processing, have gained prominence for their efficiency [14]. Previous studies have demonstrated the viability of this method. Halkaci

---

[*] Corresponding author. Email: sampurno@its.ac.id, phone: +62 85101707068

et al. utilized image processing to evaluate the form error of semi-spherical electrodes, confirming the method's sufficient accuracy [15]. Similarly, Gehri et al. applied automatic image processing to measure crack on quasi-brittle materials with low error rates [16]. Furthermore, Bergs et al. successfully monitored tool wear detection using image processing algorithms [17].

Despite these advancements, there is limited comparative analysis regarding the dimensional accuracy of EDM-induced defects specifically on the complex geometries of turbine blades [18]. This study aims to analyze the geometrical error of artificial defects fabricated by Die-Sinking EDM, specifically distinguishing between dovetail and airfoil surfaces. Using digital image processing, this research evaluates the measurement accuracy and precision of length, width, depth, and position against reference dimensions to validate the reliability of this inspection method on complex turbine components.

2. Experimental theoretical method

2.1. Materials and Equipment

The main specimen utilized in this research was a gas turbine blade obtained from a PT PLN Gas Power Plant (PLTG), which was transformed into a calibration block to evaluate the accuracy of flaw size and position. The material is characterized by high hardness and complex geometry, necessitating non-conventional machining processes. The artificial defects were fabricated using a Die-Sinking EDM machine [19]. Figure 1 below shows the gas turbine blade specimen.

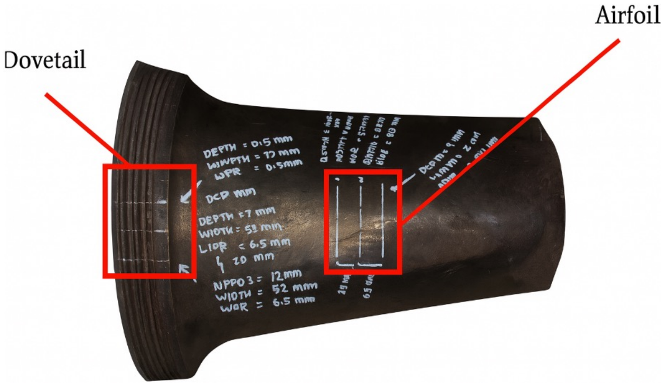

Figure 1. The gas turbine blade specimen.

For data acquisition, the imaging setup consisted of a DSLR camera Canon EOS 700D equipped with an 18-55 mm kit lens. The camera features an 18 MP sensor, a minimum shutter speed of 1/4000 sec, and a resolution of 1456×2592 pixels. A digital micrometer was also employed for validatory measurements.

2.2. Fabrication of Artificial Defects

Six artificial defects were machined onto the turbine blade to simulate varying damage conditions. These defects were categorized based on surface geometry into two distinct groups. The first group consisted of defects numbered 1, 2, and 3 located on the dovetail section, featuring a length of 57 mm and a width of 0.5 mm. The second group comprised defects numbered 4, 5, and 6 situated on the airfoil section, with dimensions of 50 mm in length and 0.5 mm in width. To investigate the influence of defect severity, three specific depth variations were applied to each group. Defects 1 and 4 were machined to a depth of 0.5 mm, defects 2 and 5 to 1.0 mm, and defects 3 and 6 to 2.0 mm. These millimeter-scale defect sizes are consistent with commonly used reference reflectors/defect size ranges in nondestructive evaluation studies [20]. The comprehensive dimensional specifications and locations for all artificial defects are presented in Figure 2.

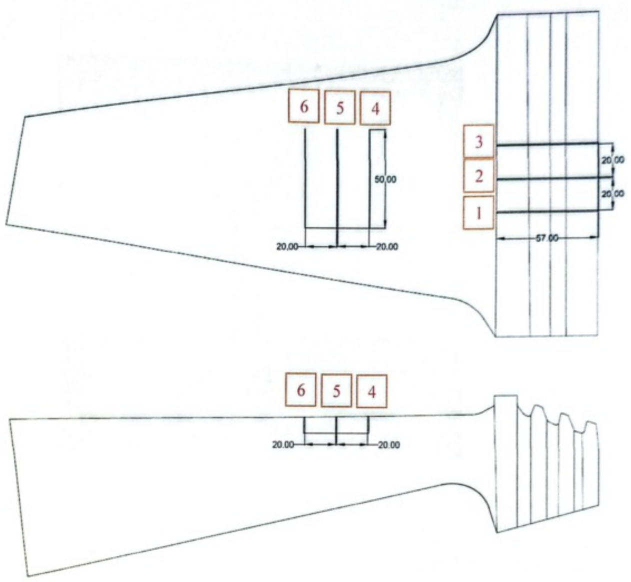

Figure 2. Location of artificial defects on the gas turbine blade.

The defects were designed as notch-type discontinuities to emulate measurable geometric damage parameters (length, width, depth, and position) that are required in practical inspection and repair screening. Die sinking EDM was selected because it enables the fabrication of repeatable notch geometries on high-hardness blade materials with controlled dimensions for metrology validation.

2.3. Image Acquisition and Processing

The image acquisition process was conducted in a controlled environment to minimize noise. The camera was mounted on a tripod at a fixed distance of 30 cm from the specimen. Lighting intensity and camera settings ISO and shutter speed were optimized to ensure image clarity. Figure 3 shows the camera setup. To achieve high precision and accuracy, the camera system underwent meticulous calibration using a standard ruler of known dimensions. Initially, the ruler was positioned at the identical focal distance and orientation as the artificial defects on the turbine blade to eliminate any perspective distortion. To ensure optimal edge detection during this calibra-

Figure 3. Camera setup.

tion process, the image was captured with optimized camera settings specifically, minimizing ISO and selecting an appropriate aperture to reduce noise and enhance detail accuracy [21], as corroborated by recent studies on optimal camera configurations. The achievable dimensional accuracy in image-based metrology is strongly influenced by the imaging configuration, particularly camera resolution, magnification, and setup conditions [22]. Upon acquiring the high-fidelity image, the Set Scale function in ImageJ software was employed. By defining the precise pixel length corresponding to the known physical dimension of the ruler, a highly accurate pixel-to-millimeter conversion ratio was established. This specific ratio was then consistently applied to calculate the true physical dimensions of the artificial defects.

During the process of image acquisition, the optical axis of the camera was precisely aligned to be perpendicular to the base plane of the workpiece. Nevertheless, the intricate surface curvature of the turbine blade, particularly within the airfoil region, may result in the local surface of the defect being inclined at an angle α relative to the camera's sensor plane. Such tilt effects are known to influence the metric fidelity of image-based reconstructions and scaling and therefore must be considered when interpreting projected measurements on non-planar surfaces [23]. To account for this surface inclination and ensure accurate calculation of the result, it is necessary to geometrically correct the projected length on the image using the cosine function to ascertain the actual physical length.

$$L_{actual} = \frac{L_{projected}}{\cos(\alpha)} \tag{1}$$

In addition to the correction of the surface angle, the inherent 30 cm working distance significantly affects measurement resolution. Geometrically, an increased working distance enlarges the field of view, thereby reducing the spatial resolution ratio (mm/pixel). The effect of photography distance on achievable geometric accuracy has been quantitatively demonstrated in high-precision imaging and photogrammetry studies [24]. Capturing macro images at reduced working distance is fundamentally more precise due to finer pixel-to-millimeter resolution and reduced sensitivity to geometric distortions [22, 24].

A minimum of 20 images were captured for each defect to ensure statistical significance. The captured images were processed using ImageJ software through several systematic stages. First, the original RGB images were converted into 8-bit grayscales to simplify the processing workflow. Second, a thresholding technique was applied to perform binarization, allowing clear separation of the defect region from the background, resulting in a binary image. Third, noise-reduction operations such as Fill Holes and Close were employed to remove grain noise and minor artifacts. Finally, calibration was performed using the Set Scale function, where the pixel-to-millimeter ratio was determined based on a reference scale included within the image frame.

After calibration, dimensions were extracted in ImageJ from the cleaned binary mask. The defect boundary was used as the measurement reference and the defect axis was set along its dominant direction. Defect length was measured between the two end points along this axis using the Segmented Line tool, while defect width was measured edge-to-edge on lines perpendicular to the axis; three width readings were averaged for each defect. The same threshold settings and measurement protocol were applied across all repeats.

2.4. Destructive Testing and Data Analysis

To validate the depth measurements and internal geometry, the blade was sectioned using Wirecut EDM. Cross-sectional cuts were made at five points along each defect. Here Figure 4 below shows the workpiece cutting path with Wirecut EDM.

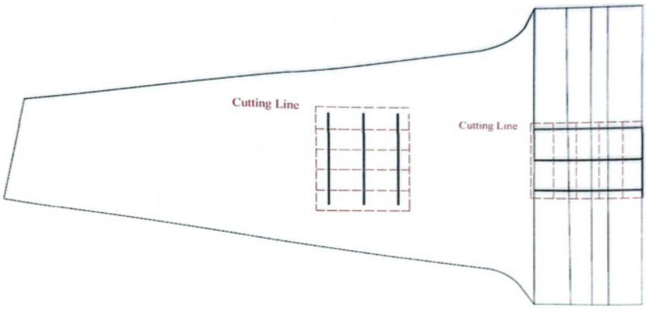

Figure 4. The workpiece cutting path with Wirecut EDM.

(a) Dovetail **(b)** Airfoil

Figure 5. Visual comparison of artificial defects on the dovetail (1–3) and airfoil (4–6).

Dimensional accuracy was evaluated by calculating the Relative Error (RE) between the measured value from image processing and the actual reference value.

$$\text{Relative Error}(\%) = \left| \frac{x_{measured} - x_{reference}}{x_{reference}} \right| \times 100 \quad (2)$$

Precision was assessed using Standard Deviation (SD) to analyze data dispersion.

$$\text{SD} = \sqrt{\frac{\sum (x_i - \overline{x})^2}{n-1}} \quad (3)$$

To statistically evaluate the effect of surface curvature on measurement accuracy, analyses were performed using Minitab. The Anderson-Darling test was used to check normality. Since the data followed a non-normal distribution, a Mann-Whitney test was employed to compare accuracy between dovetail and airfoil surfaces. Additionally, Levene's Test was used to analyze variance, and a Paired t-Test was conducted to validate the image processing results against digital micrometer measurements.

3. Result and Discussion

3.1. Visual Analysis of Artificial Defects

Visual inspection of the defects created by die-sinking EDM revealed distinct geometric characteristics owing to variations in the surface profiles. Visual comparison shows that Defects 1, 2, and 3, located in the dovetail region, exhibit sharp, well-defined edges, although Defect 1 has some imperfections in its erosion process. The jagged and contoured pattern in this region creates non-uniform light scattering, resulting in shadows that force the edge detection algorithm to adjust the image contrast during the image processing stage. In contrast, defects 4, 5, and 6, located in the airfoil region, have a significant surface curvature. This geometry creates a light reflection. Consequently, advanced noise reduction operations, such as the Fill Holes and Close functions, are required to effectively isolate the defect geometry from the background noise caused by metal surface reflections. Here Figure 5 shows the visual comparison of artificial defect on the dovetail (1-3) and airfoil (4-6).

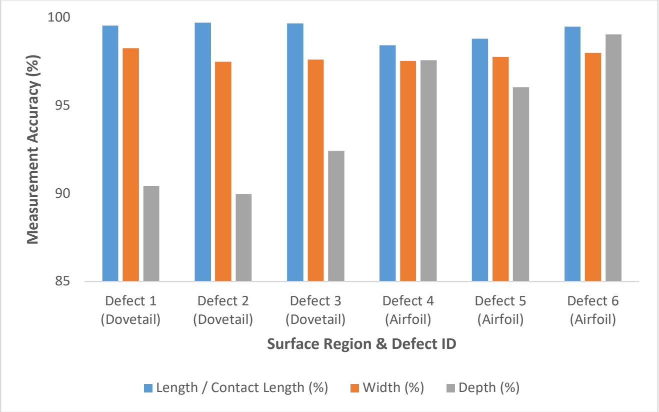

Figure 6. Comparison of measurement accuracy across all dimensions and defects.

3.2. Dimensional Accuracy Analysis

The dimensional accuracy was analyzed by calculating the Relative Error (RE) for length, width, and depth. The calculation follows the principle where a lower RE indicates higher accuracy. The measurement results are summarized in Table 1.

Based on the data in Table 1 and Figure 6, distinct trends are observed regarding measurement performance. Dovetail defects exhibit very high accuracy in length measurements (e.g., Defect 1 at 99.85%). However, a significant decrease in accuracy is observed in depth measurements, where the dovetail region only achieves approximately 90% accuracy (e.g., Defect 2 at 89.99%). This decrease in depth accuracy is scientifically attributed to the complex, jagged geometry of the dovetail root. The jagged geometry creates numerous shadows and structural edges that compete with the artificial defect boundaries. These shadows interfere with the image segmentation process, making it difficult for the algorithm to distinguish the true defect depth from geometric noise.

Table 1. Summary of target dimensions and measurement accuracy for dovetail and airfoil defects.

Geometry Type	Defect ID	Parameter	Target (mm)	Measured (mm)	Accuracy (%)
Dovetail	Defect 1	Length	57.000	56.758	99.85
		Width	0.500	0.507	98.29
		Depth	0.500	0.548	90.43
	Defect 2	Length	57.000	56.863	99.74
		Width	0.500	0.506	97.51
		Depth	1.000	0.901	89.99
	Defect 3	Length	57.000	56.899	99.7
		Width	0.500	0.509	97.65
		Depth	2.000	1.866	92.44
Airfoil	Defect 4	Length	50.000	50.775	98.45
		Width	0.500	0.511	97.55
		Depth	0.500	0.507	97.59
	Defect 5	Length	50.000	50.583	98.83
		Width	0.500	0.511	97.78
		Depth	1.000	0.966	96.07
	Defect 6	Length	50.000	50.238	99.5
		Width	0.500	0.510	98.02
		Depth	2.000	1.996	99.08

In contrast, the Airfoil region, despite its curvature, achieves a much higher depth accuracy of 99.08% (Defect 6). The smooth, continuous surface of the airfoil minimizes local shadows, providing cleaner background contrast, allowing the image processing algorithm to detect defect depth with greater precision.

3.3. Statistical Comparative Analysis

To thoroughly examine how surface geometry influences measurement accuracy, a statistical analysis was conducted using Minitab software. This analysis utilized the complete raw data set consisting of 20 repeated measurements for each of the six artificial defects, resulting in a total sample size of $n = 120$ data points. This substantial sample size ensured strong statistical power for hypothesis testing. Initial data verification using the Anderson-Darling test indicated that the error distribution for the dovetail region was non-normal with P value < 0.05. Consequently, non-parametric test was used for comparative. Here Figure 7 below shows repeatability analysis comparing 20 successive depth measurements on dovetail and airfoil surfaces at defect 3 depth and defect 6 depth.

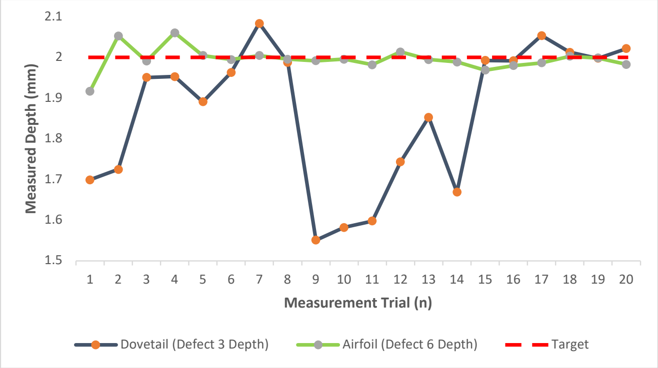

Figure 7. Repeatability analysis comparing 20 successive depth measurements on dovetail and airfoil surfaces at defect 3 depth and defect 6 depth.

To test the hypothesis that surface curvature decreases measurement accuracy, a Mann-Whitney U test was performed to compare the median errors of the two groups. The analysis yielded a P value of 0.577. Since the P value > 0.05, the null hypothesis was accepted, indicating no statistically significant difference in measurement accuracy between the dovetail and airfoil surfaces. This finding confirms that the proposed image processing algorithm is robust and maintains high accuracy regardless of the underlying surface geometry.

However, a significant difference was observed in measurement precision. Levene's test for equality of variance yielded a P value < 0.001, indicating a statistically significant difference in data variability. Contrary to the initial assumption that the dovetail region would yield better consistency, the results show that measurements in

Table 2. Comparison of measurement results obtained by image processing and micrometer measurements.

Geometry Type	Defect ID	Image Processing (mm)			Micrometer (mm)		
		Length	Width	Depth	Length	Width	Depth
Dovetail	Defect 1	56.758	0.507	0.548	56.794	0.492	0.486
	Defect 2	56.863	0.506	0.901	56.848	0.491	0.926
	Defect 3	56.899	0.509	1.866	56.886	0.493	1.958
Airfoil	Defect 4	50.775	0.511	0.507	49.971	0.491	0.495
	Defect 5	50.583	0.511	0.966	48.743	0.490	0.966
	Defect 6	50.238	0.510	1.996	49.783	0.492	1.965

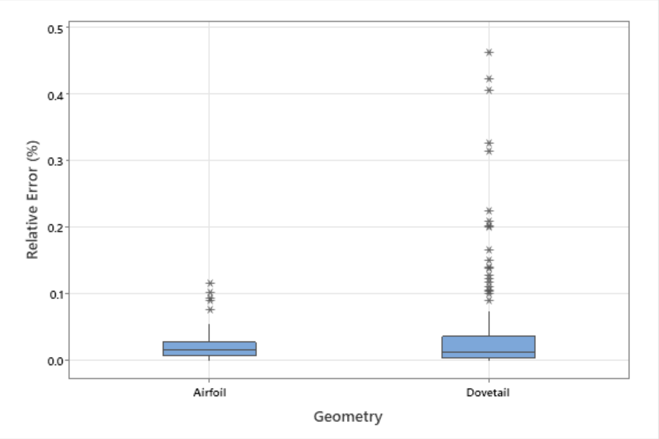

Figure 8. Boxplot comparison of measurement errors between dovetail and airfoil surfaces.

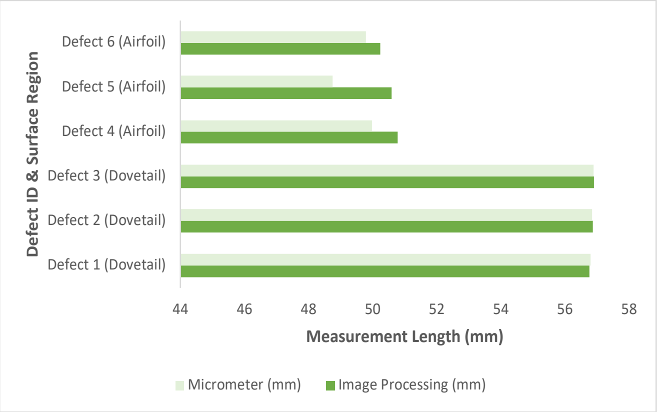

Figure 9. Comparison of dimensional measurements between the proposed image processing method and a digital micrometer.

this region are significantly less precise than those in the airfoil region.

As illustrated in the boxplot in Figure 8, the interquartile range for the dovetail region is significantly wider than that for the airfoil region. This phenomenon is attributed to the complex surface topology of the dovetail region. Unlike a simple flat surface, this region has a jagged profile with a curvature. This geometric condition creates non-uniform lighting and shadow zones that compete with the edges of artificial defects during the segmentation process. As a result, the algorithm struggles to isolate defect boundaries consistently. In contrast, the airfoil surface exhibits a smooth and continuous curvature without abrupt ridge transitions. This surface characteristic allows for a uniform lighting gradient against the background, thus enabling the thresholding algorithm to detect the defect edges with greater stability and precision.

3.4. Method Validation

To validate the reliability of the proposed image processing method, the measurement results were compared with manual measurements taken using a standard digital micrometer with 0.001 mm resolution. It is crucial to acknowledge that the image processing software calculates dimensions by multiplying pixel counts with a calibration ratio, which inherently produces mathematical outputs with multiple decimal places. However, these trailing digits are merely computational artifacts and do not reflect the actual physical spatial resolution of the camera sensor. To adhere to standard metrological principles and ensure a fair comparison, all image processing results have been systematically rounded to three decimal places. This aligns the data with the maximum physical resolution limit of the standard digital micrometer used for validation, which is 0.001 mm. Table 2 presents a comparison of the mean values for selected defects on both dovetail and airfoil surfaces.

A detailed observation of Table 2 reveals a very high agreement between the two measurement methods for the dovetail region. The absolute differences in length measurements for Defects 1, 2, and 3 are extremely minimal, ranging from only 0.013 mm to 0.036 mm. This confirms that the developed image processing algorithm is highly accurate and directly comparable to physical contact measurements when evaluating relatively straight-line features.

In contrast, notable numerical discrepancies appear in the contact length measurements of the airfoil region (e.g., a 1.840 mm deviation on Defect 5). This deviation is scientifically attributed to the fundamental limitation of using a linear contact tool on a highly contoured surface, rather than an error in the image processing algorithm. Here Figure 9 below shows comparison of dimensional measurements between the proposed image processing method and a digital micrometer.

The digital micrometer, operating as a linear contact instrument, measures the shortest straight-line distance between the two extreme ends of the defect. Conversely, the image processing method captures the two-dimensional projection of the curved surface, which more accurately approximates the true surface arc of the airfoil profile. Therefore, rather than indicating inaccuracy, this discrepancy highlights the advantage of the non-contact image processing method, as it provides a more representative evaluation of the defect's true physical span on complex turbine geometries than conventional linear instruments.

4. Conclusions

This study conducted a comparative analysis of the dimensional accuracy and precision of artificial defects created by die-sinking EDM on dovetail and airfoil surfaces of gas turbine blades, utilizing digital image processing. Based on the experimental data and statistical analysis, the following conclusions are presented:

1. The image processing method exhibited robust dimensional accuracy for both surface geometries, achieving an average accuracy exceeding 95% for planar features. Statistical analysis employing the Mann-Whitney U test (P-value = 0.577) indicated no significant difference in measurement accuracy (median error) between the dovetail and airfoil surfaces. This finding suggests that the proposed method is robust and capable of measuring defects on complex turbine geometries without significant bias.
2. While accuracy remained consistent, the precision of the measurements was significantly affected by the fundamental surface geometry. Levene's test for equality of variances (P-value < 0.001) revealed a highly statistically significant difference in variance. Measurements on the smooth airfoil region demonstrated much greater precision than those on the dovetail region. This finding is scientifically attributed to the complex, serrated geometry of the dovetail root, which creates multiple cast shadows and specular reflections that interfere with the algorithm's edge detection, making it more susceptible to geometric noise.
3. Regarding method validation, the proposed image processing technique was benchmarked against contact measurements using a digital micrometer. Deviations were negligible in the dovetail region. On the contoured airfoil, differences arose because the micrometer measures a straight chord, whereas the optical method captures a more representative projected profile length. Overall, the developed non-contact method is a reliable and efficient alternative for defect inspection in gas turbine blades, supporting practical maintenance and quality control in power generation.

Acknowledgments

The authors would like to express their gratitude to the Mechanical Engineering Department, Institut Teknologi Sepuluh Nopember, Surabaya, Indonesia.

References

[1] S. Barella, M. Boniardi, S. Cincera, P. Pellin, X. Degive, and S. Gijbels, "Failure analysis of a third stage gas turbine blade," *Engineering Failure Analysis*, vol. 18, no. 1, pp. 386–393, 2011.

[2] M. Katinić, D. Kozak, I. Gelo, and D. Damjanović, "Corrosion fatigue failure of steam turbine moving blades: A case study," *Engineering Failure Analysis*, vol. 106, p. 104136, 2019.

[3] A. Arabkoohsar and M. Sadi, "Thermodynamics, economic and environmental analyses of a hybrid waste–solar thermal power plant," *Journal of Thermal Analysis and Calorimetry*, vol. 144, no. 3, pp. 917–940, 2021.

[4] S. Zhang *et al.*, "UAV based defect detection and fault diagnosis for static and rotating wind turbine blade: a review," *Nondestructive Testing and Evaluation*, vol. 40, no. 4, pp. 1691–1729, 2025.

[5] M. Y. Izzuddin, A. Syaifudin, M. F. Rahmat, and Suwarmin, "Finite element-based fatigue analysis of medium-speed train car structure," *International Review of Mechanical Engineering*, vol. 19, no. 9, pp. 472–483, 2025.

[6] A. Syaifudin, Z. Z. Averil, M. Y. Izzuddin, A. Rasyida, S. Nurkhamiddah, L. Hakim, and K. Sasaki, "How mechanical properties of ureteral stent material affect its service life," *Journal of Biomedical Materials Research Part B: Applied Biomaterials*, vol. 113, no. 11, p. e35692, 2025.

[7] J. Lario, J. Mateos, F. Psarommatis, and Á. Ortiz, "Towards zero defect and zero waste manufacturing by implementing non-destructive inspection technologies," *Journal of Manufacturing and Materials Processing*, vol. 9, no. 2, p. 29, 2025.

[8] I. Lysenko, Y. Kuts, V. Uchanin, Y. Mirchev, and O. Levchenko, "Evaluation of eddy current array performance in detecting aircraft component defects," *Transactions on Aerospace Research*, vol. 2024, no. 2, pp. 1–9, 2024.

[9] A. Wahjudi *et al.*, "The application of hybrid BPNN and GA in the dry machining end-milling process of aluminum alloy," *International Review of Mechanical Engineering*, vol. 19, no. 1, pp. 1–15, 2025.

[10] C. S. Rubi *et al.*, "Comprehensive review on wire electrical discharge machining: a non-traditional material removal process," *Frontiers in Mechanical Engineering*, vol. 10, p. 1322605, 2024.

[11] A. P. Markopoulos, E.-L. Papazoglou, and P. Karmiris-Obratański, "Experimental study on the influence of machining conditions on the quality of electrical discharge machined surfaces of aluminum alloy Al5052," *Machines*, vol. 8, no. 1, p. 12, 2020.

[12] P. Zuo, Z. Dou, H. Yang, H. Hou, and Y. Zheng, "Enhancement of resistance to cracking under thermal cycling of EDM-treated H13 steel by shot peening with optimized intensity," *Engineering Failure Analysis*, vol. 187, p. 110622, 2026.

[13] D. Kim, U. Gerstberger, M. Asli, and K. Höschler, "U-Net driven semantic segmentation for detection and quantification of cracks on gas turbine blade tips," *Results in Engineering*, vol. 29, p. 108864, 2026.

[14] N. Ahuja, U. Batra, and K. Kumar, "Experimental investigation and optimization of wire electrical discharge machining for surface characteristics and corrosion rate of biodegradable Mg alloy," *Journal of Materials Engineering and Performance*, vol. 29, no. 6, pp. 4117–4129, 2020.

[15] H. S. Halkaci, Ö. Mavi, and O. Yigit, "Evaluation of form error at semi-spherical tools by use of image processing," *Measurement*, vol. 40, no. 9–10, pp. 860–867, 2007.

[16] N. Gehri, J. Mata-Falcón, and W. Kaufmann, "Automated crack detection and measurement based on digital image correlation," *Construction and Building Materials*, vol. 256, p. 119383, 2020.

[17] T. Bergs, C. Holst, P. Gupta, and T. Augspurger, "Digital image processing with deep learning for automated cutting tool wear detection," *Procedia Manufacturing*, vol. 48, pp. 947–958, 2020.

[18] J. E. A. Qudeiri, A. Zaiout, A.-H. I. Mourad, M. H. Abidi, and A. Elkaseer, "Principles and characteristics of different EDM processes in machining tool and die steels," *Applied Sciences*, vol. 10, no. 6, p. 2082, 2020.

[19] C. G. Camerini *et al.*, "Correlation of eddy current signals obtained from EDM notches and fatigue cracks," *Journal of Materials Research and Technology*, vol. 8, no. 5, pp. 4843–4848, 2019.

[20] X. Lei, H. Wirdelius, and A. Rosell, "Simulation-based investigation of a probability of detection (POD) model using phased array ultrasonic testing (PAUT) technique," *Journal of Nondestructive Evaluation*, vol. 41, no. 2, p. 40, 2022.

[21] D. Rangelov, S. Waanders, K. Waanders, M. van Keulen, and R. Miltchev, "Impact of camera settings on 3D reconstruction quality: Insights from NeRF and gaussian splatting," *Sensors*, vol. 24, no. 23, p. 7594, 2024.

[22] G. Póka and B. Z. Balázs, "A robust digital image processing method for measuring the planar burr length at milling," *Journal of Manufacturing Processes*, vol. 80, pp. 706–717, 2022.

[23] P. Kozikowski, "Extracting three-dimensional information from SEM images by means of photogrammetry," *Micron*, vol. 134, p. 102873, 2020.

[24] J. Liu, S. Ma, R. Chen, C. Han, Y. Li, K. Ma, and Y. Zhang, "Influence of photography distance and image network geometry on ground-based SfM photogrammetry accuracy," *Research in Cold and Arid Regions*, 2025. In Press, Corrected Proof; available online 20 November 2025.